Radio Interferometric Imaging Algorithms - 2018.

Urvashi Rau[a]

[a]National Radio Astronomy Observatory, 1003 Lopezville Road, Socorro, U.S.A.

This note summarizes the key ideas involved in radio interferometric data analysis and image reconstruction, and lists a series of references to algorithms documented in current literature as of Summer 2018.

1. DATA ACQUISITION

Each pair of antennas measures the degree of spatial correlation of the electric field incident at the locations of the two antennas by computing the product of the voltage streams from one pair of antennas and integrating it over a short timespan and narrow frequency range (over which phase coherence is preserved). An ideal complex visibility measured by the antenna pair i, j can be written as ${V^{obs}}_{ij} = \langle E_I E_J^* \rangle$.

In practice, each measurement is a 4-vector representing all possible products from the pair of orthogonal feeds (detectors) present on each antenna and corrupted by the measurement process.

$$\vec{V}_{ij}^{obs} = \langle \vec{E}_i^{obs} \otimes \vec{E}_j^{obs^*} \rangle = \langle [J_i]\vec{E}_i \otimes [J_j]^* \vec{E}_j^* \rangle = ([J_i] \otimes [J_j]^*) \langle \vec{E}_i \otimes \vec{E}_j^* \rangle = [K_{ij}]\vec{V}_{ij} \tag{1}$$

where $[J_i]$ represents a cumulative Jones matrix[1–3] that describes the modulation imposed upon the two orthogonal axes of the incoming E-field during measurement.

The ideal van Cittert Zernike theorem describing the 2D Fourier relation between the sky brightness and the sampled visibilities can be combined with the effect of the full-polarization measurement process from Eqn. 1 to describe the visibility measured by baseline ij at one instant in time and at one frequency.

$$\vec{V}_{ij}^{obs}(u,v) = \left[K_{ij}^{vis}\right] \iint \left[K_{ij}^{sky}(l,m)\right] \vec{I}^{sky}(l,m)\ e^{-2\pi i(ul+vm)} dldm \tag{2}$$

Here, $\vec{I}^{sky}(l,m)$ is a 4×1 vector of the sky brightness distribution (in the direction l, m) corresponding to either the four correlation pairs or the four Stokes parameters. u, v represents the spatial frequency sampled by baseline ij at one instant in time. $[K_{ij}^{vis}]$ is a 4×4 matrix that represents direction-independent instrumental effects that are constant across the field of view of each antenna (*e.g.* receiver gains). $[K_{ij}^{sky}(l,m)]$ is a 4×4 matrix per direction on the sky and it represents effects that vary with position on the sky (*e.g.* antenna primary beams, pointing offsets, ionospheric effects and geometrical effects due to sky curvature and the non-coplanarity of the array). When $\vec{I}^{sky}(l,m)$ represent the four Stokes parameters $[K_{ij}^{vis}]$ is a Mueller matrix.

The effect of $K_{ij}^{sky}(l,m)$ in Eqn. 2 is multiplicative in the image domain and can be represented as a convolution in the visibility domain. Let $K_{ij}^{dd}(u,v)$ represent the Fourier transform of $K_{ij}^{sky}(l,m)$ (for each of the four correlation pairs). Eqn. 2 can be re-written as follows with $\star$ representing convolution for each correlation product.

$$\vec{V}_{ij}^{obs}(u,v) = \left[K_{ij}^{vis}\right] \left\{ \left[K_{ij}^{dd}(u,v)\right] \star \iint \vec{I}^{sky}(l,m)\ e^{-2\pi i(ul+vm)} dldm \right\} \tag{3}$$

Eqns. 2 and 3 describe the measurement equation for one visibility. In practice, $\vec{V}_{ij}^{obs}$ is measured for all $\frac{N_a(N_a-1)}{2}$ pairs of antennas ($i = 1 - N_a$ and $j = i - N_a$) for a series of integration timesteps and observing frequencies, with up to four possible correlation products from each antenna pair.

Associated with each data point is also a weight, sometimes derived from known instrumental characteristics and sometimes estimated during post-processing. Additionally, as radio telescopes operate at wavelengths where there are plenty of man made communication signals and significant fractions of data can be affected by this radio frequency interference. These corrupted data points must first be identified and then discarded or masked prior to further processing. The practical result is that there will be gaps in the observations in time, freq as well as non-uniform data weights.

The solution of Eqn. 3 for all baselines, times and frequencies involved in an observation is typically done in two steps, calibration and imaging, sometimes involving iterations between the two.

2. SELF-CALIBRATION

The process of self-calibration uses observed visibilities from a known source (i.e. V^{true} is known) to solve for direction independent antenna-based complex gain solutions that form the $[K^{vis}]$ matrix* from Eqn. 3. The following system of equations (written per antenna pair i, j) is solved via an iterative non-linear least squares optimization†.

$$\vec{V}_{ij}^{obs} = [{K^{vis}}_{ij}]\vec{V}_{ij} \text{ where } [{K^{vis}}_{ij}] = ([J_i] \otimes [J_j]^*) \tag{4}$$

The antenna-based calibration solutions $[J_i]$ thus obtained are then applied to the observed data by constructing and applying the inverse of $[{K^{vis}}_{ij}]$. A typical observation includes data from a known calibrator source, interleaved in time with observations of the target. Gain solutions are calculated using the calibrator data and then interpolated across the time ranges for which the target data must be calibrated. Sometimes, self-calibration is performed on the target sky being imaged, in which case several iterations of calibration and imaging may be done to successively refine both the calibration solutions as well as the image model.

Different instrumental effects are also usually handled separately in ways that maximize the signal-to-noise ratio available to the solvers for each effect. For example, the spectral bandpass of the receiver is typically stable across a few hour timescale. Therefore data from (say) 2 hours of observation may be used to derive a single amplitude gain solution. On the other hand, phase stability may vary on a timescale of 10 minutes but be consistent across frequency. In this case, gain solutions must be derived every few minutes but data from multiple frequency channels may be used together to obtain a single number for the entire spectrum. A series of calibration solutions and applications is typically performed for different physical reasons. Note that given the structure of eqn. 4, it is possible to also perform a direct inversion of $[K^{vis}]$ to derive corrections without the formal constraint of the solution being a fundamentally antenna-based number, but this approach must be used with abundant caution and only for well-understood and specific baseline-based errors.

2.1 Direction dependent effects

Direction dependent antenna-based effects arise from the physical shape and illumination pattern of each element of the array (e.g. pointing, defocus, etc), geometrical effects relating to the sky curvature and non-coplanarity of the array elements, and position dependent refraction effects due to ionospheric turbulence. As seen from Eqns. 2 and 3, these effects can be modeled per antenna pair as either as convolutions in the visibility domain or as multiplicative image domain effects, and this leads to two classes of algorithms to deal with them.

Projection methods[4,5] apply wide-field instrumental corrections during image formation by carefully constructing convolution functions to use when resampling the visibility data onto a regular grid prior to the the FFT that forms the observed image. These baseline and time-dependent convolution functions are chosen to cancel out the effect of $[K^{sky}]_{ij}$. For example, the W-Projection[4] algorithm uses Fresnel kernels to derive convolution functions that compensate for the non-coplanarity of measurements on a single spatial frequency plane. The AW-Projection[5] algorithm derives convolution functions using models of the aperture illumination function of each antenna in the array, corrects for known pointing offsets, and accounts for variability of these antenna patters across time and baseline. These primary beam effects can be combined with W-term effects as well. The WB-AWProjection[6] algorithm additionally applies an approximate correction for the frequency dependence of the instrumental primary beam as well. A full-polarization equivalent of A-Projection[7] applies corrections for the full Mueller matrix for use in wide-field full-polarization imaging. Higher order corrections using models that describe the effective aperture illumination function due to ionospheric refraction have also been demonstrated. These algorithms typically use physically motivated models of the various effects that can be derived theoretically for geometrical corrections for wide-field non-coplanar effects or from measured holography data to characterize antenna primary beams.[5,8] Joint mosaic imaging[9] is a related area where these algorithms apply.

*This step typically ignores direction dependent effects represeted by $[K^{vis}]$ or applies some pre-computed model. Sec.2.1 describes algorithms that handle direction dependent terms

†Self-calibration solutions are related to performing an eigen value decomposition of the visibility correlation matrix when there is only one dominant compact source in the field of view (or when the visibilities in the matrix represent V^{obs}/V^{true}).

For effects that cannot be pre-computed because they vary in unpredictable ways, algorithms such as SAGE[10,11] and DD-Facets[12] solve for direction-independent calibration solutions simultaneously in multiple directions, typically towards all the brightest sources in the field of view. These algorithms often solve both for calibration parameters and the sky model parameters iteratively in a self-calibration loop. Algorithms also exist that model the variability in terms of physical antenna-based parameters and then iteratively solve for these parameters from the data themselves. Pointing self-calibration[13] is one such idea that derives and applies corrections for antenna based pointing offsets (which can be related to the first order terms of a Zernicke polynomial expansion of the aperture illumination phase structure).

3. IMAGING

Eqn. 2 can be written in discretized form[14] with the true sky brightness distribution represented as a 1D vector ${I^{sky}}_{mx1}$, a set of observed visibilities ${V^{obs}}_{nx1}$ and a measurement operator $[A_{nxm}]$.

$$V^{obs} = [K^{vis}][S][F][K^{sky}]I^{sky} \tag{5}$$

Here, $[S]$ represents the spatial frequency sampling function, $[F]$ is the Fourier Transform operator and $[K^{vis}]$ and $[K^{sky}]$ represent direction independent and direction dependent instrumental (calibration) effects. In this system of equations, only $[S]$, $[F]$, $[V^{obs}]$ and an associated set of data weights $[W]$ are known. Calibration for direction independent effects eliminates $[K^{vis}]$ and for the purpose of image reconstruction we can assume that a model of $[K^{sky}]$ is also available.

A sky brightness model is therefore reconstructed from iteratively solving the following system of equations.

$$V^{obs} = [A]I^{model} = [S][F][K^{sky}]I^{model} \tag{6}$$

An L2 minimization results in the following set of normal equations

$$[A^{\dagger}W]V^{obs} = [A^{\dagger}WA]I^{model} \tag{7}$$

The model is then iteratively built up as

$${I^{model}}_{i+1} = {I^{model}}_{i} + g[A^{\dagger}WA]^{+}\left(A^{\dagger}W\left[V^{obs} - A{I^{model}}_{i}\right]\right) \tag{8}$$

In equations 7 and 8, $[K^{sky}]$ is either approximated as an invariant term that can be combined with the sky model being solved for (i.e. as part of I^{model}) or incorporated within $[A]$ to handle effects that differ across baselines, frequency or time. In the latter situation, projection algorithms mentioned in Sec. 2.1 apply corrections as part of the $[A^{\dagger}W]$ operator such that an average version of $[K^{sky}]$ can still be factored out of the normal equations and treated as part of the model.

With these simplifying assumptions, $[A^{\dagger}WA]$ is a convolution operator.[14] Therefore, Eqn. 7 describes the convolution of the sky brightness distribution with a point spread function given by the spatial frequency sampling function and weights. $[A^{\dagger}W]$ is the data-to-image transform and $[A]$ is the forward model used to compute visibilities to compare with the measured data. The data-to-image transform involves a convolutional resampling (called gridding) to transfer a list of weighted visibilities onto a regular spatial frequency grid, prior to an FFT that forms the observed image. The model-to-data transform does the reverse degridding operation by evaluating model visibilities that can then be compared with the original data to compute residuals. Various derivations of $[W]$ are used in weighting schemes that precondition the normal equations prior to their solution.

The update step in Eqn. 8 involves calculating an approximate inverse of the Hessian matrix $[A^{\dagger}WA]$. As the spatial frequency sampling is incomplete, this Hessian is a singular matrix with no unique inverse. Therefore, the solution to Eqn.7 is itself a non-linear optimization problem defined in the image domain. In its simplest form, a pseudo-inverse derived from a diagonal approximation is used to normalize the observed image before a greedy algorithm like CLEAN identifies flux components as delta functions at the locations of the peaks.

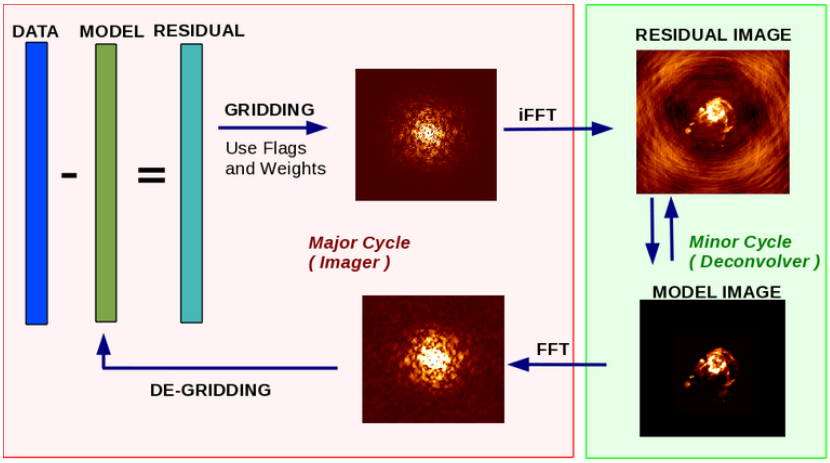

Figure 1. Image reconstruction follows a global iterative L2 minimization scheme with the update direction being calculated by any non-linear image-domain optimization schemes. The data-to-image transform involves gridding the irregularly sampled visibilties onto a regular grid prior to an iFFT and the model-to-data transform predicts visibilities from the current best estimate of the sky model. The sky model solvers in the minor cycle are free to employ a wide variety of non-linear parameterizations and optimization strategies.

3.1 Imaging Framework

Radio interferometric image reconstruction is typically implemented in a framework that consists of a pair of nested loops as illustrated in Fig. 1. The data-to-image and model-to-data steps form the *major cycle* and the derivation of model parameters from the observed (and residual) image is called the *minor cycle*. In the context of the global L2 minimization described in Eq.8, the minor cycle is what computes the update step and the major cycle reconciles this new model with the data to compute a new residual image. The non-linear image-domain optimization algorithm implemented as the minor cycle can include a variety of sky parameterizations and optimization strategies, some of which are listed in Sec. 3.2. There are also a variety of gridding algorithms, summarized in section. 2.1 that can apply corrections for different wide-field effects (for example, differences in antenna aperture illumination patterns and pointing offsets) by careful choices of gridding convolution functions.

The main reason for these nested loops is to minimze the computational load incurred if $[A^{\dagger}W]$ and $[A]$ is calculated for every step taken by the sky model solver. For large volumes of data, the data I/O, gridding and de-gridding steps dominate the runtime, especially if projection algorithms are employed during gridding and degridding. Modern software implementations include data partitioning for parallelization. Usually an imaging run involves on the order of 10 major cycles but depending on the minor cycle algorithm used may require anything between a few hundred to several tens of thousands of steps within each set of minor cycle iterations. Convergence is typically assessed by how closely the residual image resembles Gaussian random noise.

A key element of this reconstruction approach is that not all steps need to be accurate. The data-to-image transform may leave out some instrumental effects or only approximately correct them in order to speed up the computation of the initial residual image. Some wide-field effects (such as the construction of joint mosaics) naturally break the strict 2D Fourier transform relation making the observed image only an approximate convolution between the sky and the point spread function and therefore not a perfect fit for the model being solved for in the minor cycle. The minor cycle algorithm may itself may be approximate, using a greedy approach to the solution of the normal equations in eqn. 7, and often ignoring issues arising from wide-field approximations. In fact, it can be shown that algorithms that perform imaging in one step followed by one (iterative) deconvolution step can be quite error prone. But, with errors within reasonable limits, as long as the model-to-data transform is as accurate as possible, the global iterative (steepest descent) scheme does eventually converge to a viable solution. The other advantage of a global L2-norm solution is its appropriateness for Gaussian random noise especially when the desired astrophysics also depends on the residual noise statistics.

3.2 Image Reconstruction Algorithms

The oldest (and fastest) algorithms model the sky brightness as a collection of delta functions and use a greedy approach to finding flux components simply as delta functions at the locatons of the peaks in the normalized residual image. They usually begin with the brightest sources, subtract out their contribution to the observed image (i.e. each flux component convolved with the point spread function) and iteratively move to weaker sources upto some limit, before triggering a major cycle. Hogbom,[15] Clark[16] and Cotton-Schwab[17] CLEAN are all variants of this approach.

Algorithms such as Multi-Scale CLEAN[18] and Multi-Term Multi-Frequency-Synthesis[19] are multi-term derivations of the same global L2-norm approach. Multi-Scale Clean models the sky brightness as a linear combination of flux components at a fixed set of scale sizes (including delta function for unresolved sources). Multi-Term MFS performs joint wideband reconstructions by additionally modeling the amplitude of each multi-scale flux component as a Taylor polynomial in frequency. It is therefore able to reconstruct the intensity and spectral structure from multi-frequency data at an angular resolution given by the joint spatial frequency coverage. A multi-resolution CLEAN is another variant of such an approach as is a TV-Clean[20] that models smooth time variability in addition to multi-scale and multi-frequency models. All of these methods can be interpreted as first transforming the data and observed images into a basis or parameter space in which the signal is sparse, and then using a greedy algorithm that is well suited to such sparseness.

There are also several constrained optimization solvers that go beyond linear models. The Maximum Entropy method[21,22] uses a pixel amplitude basis and solves for L2 combined with a relative entropy term that serves to bias the solution towards externally provided a-priori information for parts of the parameter space where constraints from the data may be insufficient. The non-negative least squares[23] algorithm is another pixel-based method that solves a least squared problem with linear inequality range constraints to impose positivity of all pixels in the model. The ASP[24,25] algorithm parameterizes the sky into a collection of Gaussians and does a formal constrained optimization on their parameters using L2 as well as a TV-norm and uses sub-space selections to refine and optimize the number of components being fitted. More recently, formal compressed-sensing theory has have begun to be used to derive image reconstruction algorithms for radio interferometry.[26] The SARA[27] and PURIFY[28] algorithms use a wavelet basis and a regularization based on imposing sparsity. RESOLVE and its variants[29] are a class of algorithms derived from a Bayesian formulation and applies constraints based on log-normal statistics and desired spatial correlation structures. This algorithm is optimized for extended emission and includes wideband models as well as polarization reconstructions involving Faraday rotation. The unique contribution of this method is its ability to also produce uncertainty maps. Bayesian MCMC[30] methods have also been tried with promising results in producing uncertainty estimates, but which are computationally impractical.MORESANE[31] is another sparse deconvolution algorithm that explores more automation in choosing appropriate atome with which to model the sky brightness. As originally formulated, many of these methods rely on numerous expensive traversals through the data. However, adaptations to the practical major/minor cycle approach used in most production imaging systems, as well as alternate algorithmic formulations (such as a primal-dual formulation[32] of the convex optimization problem) to speed up and or parallelize the computation are ways in which these methods are currently becoming practical.

For mainstream practical use, all these image reconstruction algorithms must work along with direction dependent calibration approaches such as those described in Sec. 2.1. The imaging framework described in Sec. 3.1 and implemented within software packages such as CASA (https://casa.nrao.edu/casadocs) is one clear way to achieve this. The LOFAR sparse image reconstruction algorithm[33] demonstrates a practical implementation of a compressed-sensing base sparse solver within a framework similar to that described in Sec. 3.1. Alternate formulations[34] are also being explored to treat the calibration and image reconstruction process together.

Many of the above ideas can apply to optical interferometric reconstructions (and VLBI). Some sparse modeling approaches[35,36] have been analysed in the context of traditional complex visibilities as well as reconstructions from amplitudes and closure phases. This work was motivated by the imaging problem of the Event Horizon Telescope. The optical interferometric imaging community also has their own suite of experimental algorithms.[37] They have largely focused on narrow-band parametric and non-parametric Baysian approaches but have recently begun to include multi-spectral models.

4. AUTOMATED DATA ANALYSIS

The large variety of calibration schemes and image reconstruction algorithms as described above naturally leads to a situation of having to choose what is most appropriate for a given situation, especially when different algorithms can potentially give different results. The different approaches also have widely varying computational complexities and therefore choosing an approach is not simply a matter of choosing the most comprehensive techniques. The data analysis process is therefore a sequence of interactive steps involving trial and error and using intermediate results along with various rules of thumb to decide what algorithms are the most appropriate for the specific imaging problem at hand, as well as to quantify the quality and degree of umabbiguity of the final reconstructions.

In recent years, automated end-to-end data analysis pipelines have become a requirement in radio interferometry in order to deal with vast data volumes and to reduce the end user's responsibility of having to learn about and perform the entire data reduction sequence. For example, the ALMA telescope now routinely uses a pipeline to deliver science-quality data products to its users[‡]. The VLA has a calibration pipeline for general users and a specifically tuned imaging pipeline for an ongoing VLA Sky Survey [§]. These are the initial versions of such end-to-end automated systems, tuned to specific observing modes and data products, and often still involving manual intervention for troubleshooting and quality assurance. It is a topic of active ongoing research to generalize such solutions and either automate or optimize their development process.

The ability to produce reliable uncertainty maps is an another area of interest. In radio interferometry, existing techniques are very compute intensive making it impossible to run on modern radio interferometer data, but they certainly are feasible approaches for sparse coverages encountered in optical interferometry and in very long baseline radio interferometry.

REFERENCES

[1] Sault, R. J. and Cornwell, T. J., "Synthesis imaging in radio astronomy ii," in [*Astron. Soc. Pac. Conf. Ser. 180: Synthesis Imaging in Radio Astronomy II*], Taylor, G. B., Carilli, C. L., and Perley, R. A., eds. (1999).

[2] Smirnov, O. M., "Revisiting the radio interferometer measurement equation. I. A full-sky Jones formalism," *aap* **527**, A106 (Mar. 2011).

[3] Smirnov, O. M., "Revisiting the radio interferometer measurement equation. II. Calibration and direction-dependent effects," *aap* **527**, A107 (Mar. 2011).

[4] Cornwell, T. J., Golap, K., and Bhatnagar, S., "The non-coplanar baselines effect in radio interferometry: The w-projection algorithm," *IEEE Journal of Selected Topics in Sig. Proc.* **2**, 647–657 (Oct 2008).

[5] Bhatnagar, S., Cornwell, T. J., Golap, K., and Uson, J. M., "Correcting direction-dependent gains in the deconvolution of radio interferometric images," *Astron. & Astrophys.* **487**, 419–429 (Aug. 2008).

[6] Bhatnagar, S., Rau, U., and Golap, K., "Wide-field wide-band Interferometric Imaging: The WB A-Projection and Hybrid Algorithms," *apj* **770**, 91 (June 2013).

[7] Tasse, C., van der Tol, S., van Zwieten, J., van Diepen, G., and Bhatnagar, S., "Applying full polarization A-Projection to very wide field of view instruments: An imager for LOFAR," *aap* **553**, A105 (May 2013).

[8] Jagannathan, P., Bhatnagar, S., Brisken, W., and Taylor, A. R., "Direction-dependent corrections in polarimetric radio imaging. ii. a-solver methodology: A low-order solver for the a-term of the a-projection algorithm," *The Astronomical Journal* **155**(1), 3 (2018).

[9] Sault, R. J., Staveley-Smith, L., and Brouw, W. N., "An approach to interferometric mosaicing.," *aaps* **120**, 375–384 (Dec. 1996).

[10] Yatawatta, S., Zaroubi, S., de Bruyn, G., Koopmans, L., and Noordam, J., "Radio Interferometric Calibration Using The SAGE Algorithm," *ArXiv e-prints* (Oct. 2008).

[11] Kazemi, S., Yatawatta, S., and Zaroubi, S., "Clustered calibration: an improvement to radio interferometric direction-dependent self-calibration," *Monthly Notices of the Royal Astronomical Society* **430**(2), 1457–1472 (2013).

[‡]https://almascience.nrao.edu/processing/science-pipeline

[§]https://science.nrao.edu/science/surveys/vlass

[12] Tasse, C., Hugo, B., Mirmont, M., Smirnov, O., Atemkeng, M., Bester, L., Hardcastle, M. J., Lakhoo, R., Perkins, S., and Shimwell, T., "Faceting for direction-dependent spectral deconvolution," *aap* **611**, A87 (Apr. 2018).

[13] Bhatnagar, S. and Cornwell, T. J., "The pointing self-calibration algorithm for aperture synthesis radio telescopes," *The Astronomical Journal* **154**(5), 197 (2017).

[14] Rau, U., Bhatnagar, S., Voronkov, M. A., and Cornwell, T. J., "Advances in Calibration and Imaging Techniques in Radio Interferometry," *IEEE Proceedings* **97**, 1472–1481 (Aug. 2009).

[15] Högbom, J. A., "Aperture Synthesis with a Non-Regular Distribution of Interferometer Baselines," *Astron. & Astrophys. Suppl. Ser.* **15**, 417 (June 1974).

[16] Clark, B. G., "An efficient implementation of the algorithm 'clean'," *Astron. & Astrophys.* **89**, 377 (Sept. 1980).

[17] Schwab, F. R. and Cotton, W. D., "Global fringe search techniques for VLBI," *aj* **88**, 688–694 (May 1983).

[18] Cornwell, T. J., "Multi-Scale CLEAN deconvolution of radio synthesis images," *IEEE Journal of Selected Topics in Sig. Proc.* **2**, 793–801 (Oct 2008).

[19] Rau, U. and Cornwell, T. J., "A multi-scale multi-frequency deconvolution algorithm for synthesis imaging in radio interferometry," *aap* **532**, A71 (Aug. 2011).

[20] Rau, U., "Radio interferometric imaging of spatial structure that varies with time and frequency," (2012).

[21] Cornwell, T. J. and Evans, K. J., "A simple maximum entropy deconvolution algorithm," *Astron. & Astrophys.* **143**, 77–83 (1985).

[22] Narayan, R. and Nityananda, R., "Maximum entropy image restoration in astronomy," *Ann. Rev. Astron. Astrophys.* **24**, 127–170 (1986).

[23] Briggs, D. S., *High fidelity deconvolution of moderately resolved sources*, PhD thesis, The New Mexico Institute of Mining and Technology, Socorro, New Mexico, USA (March 1995).

[24] Bhatnagar, S. and Cornwell, T. J., "Scale sensitive deconvolution of interferometric images. I. Adaptive Scale Pixel (Asp) decomposition," *Astron. & Astrophys.* **426**, 747–754 (Nov. 2004).

[25] Zhang, L., Bhatnagar, S., Rau, U., and Zhang, M., "Efficient implementation of the adaptive scale pixel decomposition algorithm," *aap* **592**, A128 (Aug. 2016).

[26] Wiaux, Y., Puy, G., Boursier, Y., and Vandergheynst, P., "Compressed sensing for radio interferometry: spread spectrum imaging techniques," in [*Society of Photo-Optical Instrumentation Engineers (SPIE) Conference Series*], *Presented at the Society of Photo-Optical Instrumentation Engineers (SPIE) Conference* **7446** (Aug. 2009).

[27] Carrillo, R. E., McEwen, J. D., and Wiaux, Y., "Sparsity averaging reweighted analysis (sara): a novel algorithm for radio-interferometric imaging," *Monthly Notices of the Royal Astronomical Society* **426**(2), 1223–1234 (2012).

[28] Carrillo, R. E., McEwen, J. D., and Wiaux, Y., "Purify: a new approach to radio-interferometric imaging," *Monthly Notices of the Royal Astronomical Society* **439**(4), 3591–3604 (2014).

[29] Junklewitz, H., Bell, M. R., Selig, M., and Enßlin, T. A., "RESOLVE: A new algorithm for aperture synthesis imaging of extended emission in radio astronomy," *aap* **586**, A76 (Feb. 2016).

[30] Rau, U. and Cornwell, T. J., "Monte Carlo Image Analysis in Radio Interferometry MC-FIT: A Bayesian Approach to Object Detection," in [*Astronomical Data Analysis Software and Systems XIV*], Shopbell, P., Britton, M., and Ebert, R., eds., *Astronomical Society of the Pacific Conference Series* **347**, 168 (Dec. 2005).

[31] Dabbech, A., Ferrari, C., Mary, D., Slezak, E., Smirnov, O., and Kenyon, J. S., "MORESANE: MOdel REconstruction by Synthesis-ANalysis Estimators. A sparse deconvolution algorithm for radio interferometric imaging," *aap* **576**, A7 (Apr. 2015).

[32] Onose, A., Carrillo, R. E., McEwen, J. D., and Wiaux, Y., "A randomised primal-dual algorithm for distributed radio-interferometric imaging," *ArXiv e-prints* (Oct. 2016).

[33] Garsden, H., Girard, J. N., Starck, J. L., Corbel, S., Tasse, C., Woiselle, A., McKean, J. P., van Amesfoort, A. S., Anderson, J., Avruch, I. M., Beck, R., Bentum, M. J., Best, P., Breitling, F., Broderick, J., Brüggen, M., Butcher, H. R., Ciardi, B., de Gasperin, F., de Geus, E., de Vos, M., Duscha, S., Eislöffel, J., Engels, D., Falcke, H., Fallows, R. A., Fender, R., Ferrari, C., Frieswijk, W., Garrett, M. A., Grießmeier, J., Gunst, A. W., Hassall, T. E., Heald, G., Hoeft, M., Hörandel, J., van der Horst, A., Juette, E., Karastergiou, A., Kondratiev, V. I., Kramer, M., Kuniyoshi, M., Kuper, G., Mann, G., Markoff, S., McFadden, R., McKay-Bukowski, D., Mulcahy, D. D., Munk, H., Norden, M. J., Orru, E., Paas, H., Pandey- Pommier, M., Pandey, V. N., Pietka, G., Pizzo, R., Polatidis, A. G., Renting, A., Röttgering, H., Rowlinson, A., Schwarz, D., Sluman, J., Smirnov, O., Stappers, B. W., Steinmetz, M., Stewart, A., Swinbank, J., Tagger, M., Tang, Y., Tasse, C., Thoudam, S., Toribio, C., Vermeulen, R., Vocks, C., van Weeren, R. J., Wijnholds, S. J., Wise, M. W., Wucknitz, O., Yatawatta, S., Zarka, P., and Zensus, A., "LOFAR sparse image reconstruction," *aap* **575**, A90 (Mar. 2015).

[34] Repetti, A. and Wiaux, Y., "A non-convex perspective on calibration and imaging in radio interferometry," in [*Proceedings of the SPIE, Volume 10394, id. 103941W 13 pp. (2017).*], **10394**, 103941W (Aug. 2017).

[35] Akiyama, K., Kuramochi, K., Ikeda, S., Fish, V. L., Tazaki, F., Honma, M., Doeleman, S. S., Broderick, A. E., Dexter, J., Mościbrodzka, M., Bouman, K. L., Chael, A. A., and Zaizen, M., "Imaging the Schwarzschild-radius-scale Structure of M87 with the Event Horizon Telescope Using Sparse Modeling," *apj* **838**, 1 (Mar. 2017).

[36] Chael, A. A., Johnson, M. D., Bouman, K. L., Blackburn, L. L., Akiyama, K., and Narayan, R., "Interferometric imaging directly with closure phases and closure amplitudes," *The Astrophysical Journal* **857**(1), 23 (2018).

[37] Thiébaut, É. and Young, J., "Principles of image reconstruction in optical interferometry: tutorial," *Journal of the Optical Society of America A* **34**, 904 (June 2017).